

Graded anisotropic metamaterials for elastic wave mode conversion

Jagannadh Boddapati^{a,b}, Jihoon Ahn^a, Alexander C. Ogren^a, Chiara Daraio^a

^a*Division of Engineering and Applied Science, California Institute of Technology, Pasadena, CA 91125, USA*

^b*Intel Corporation, Santa Clara, CA 95054, USA*

Abstract

Efficient transmission of elastic waves across interfaces is central to several applications, including medical imaging, seismic isolation, and transducer design. Interfaces with abrupt changes in the material properties significantly impede wave transmission, leading to reflections. This limitation, known as impedance mismatch, becomes even more prominent for mode conversion between different wave types due to polarization mismatch. In this study, we investigate a mechanism employing two-dimensional functionally graded anisotropic metamaterials to facilitate longitudinal–shear mode conversion as waves propagate from a stiff to a compliant medium. By embedding density and anisotropic shape gradients within the functionally graded metamaterial, polarization-induced impedance mismatch is mitigated and efficient mode conversion is enabled. We use unit cell dispersion analysis to tailor the frequency range for mode conversion through gradation in the dispersion behavior and coupling between modes. Using frequency-domain finite element analysis, we demonstrate broadband mode conversion across interfaces with large stiffness contrast operating in the 1–10 kHz range. We then experimentally validate and quantify mode conversion through full-field velocity measurements on an additively manufactured specimen. We further apply the methodology to design a device capable of converting radial–tangential wave modes.

Keywords: Mode conversion, Functionally graded metamaterials, Anisotropy, Shear–normal coupling, Elastic waves

1. Introduction

Elastic waves traveling between different interfaces are ubiquitous to several applications such as medical imaging (Sarvazyan et al., 1998), structural health monitoring (Miao and Li, 2021), seismic protection (Achenbach, 1999), and sound propagation (Taljanovic et al., 2017). However, abrupt changes in the material properties at the interfaces cause strong reflections and hinder wave transmission, a phenomenon known as impedance mismatch (Liu et al., 2018). To enhance wave transmission, matching layers with intermediate impedance are often utilized (Fletcher and Thwaites, 1992; Rathod, 2020), as they provide a less abrupt change in the material properties and reduce reflections. Further, elastic waves can also undergo mode conversion, in which energy is transferred between polarizations corresponding to different deformation modes (White and Stephen, 1980; Ding et al., 2022). Efficient elastic wave mode conversion

*Corresponding author

Email address: daraio@caltech.edu (Chiara Daraio)

is crucial to applications such as ultrasound transmission through skull (Clement et al., 2004; Mazzotti et al., 2022), flow sensing (Piao et al., 2020), structural health monitoring (Miao and Li, 2021), medical needle insertion (Wang et al., 2022), nanoscale heat transfer (Shi, 2018), and more.

Despite its importance, achieving mode conversion across interfaces remains challenging because waves with different polarizations involve inherently incompatible displacement directions (Yang et al., 2019; Lee et al., 2024b). Conventional approaches to mitigate impedance mismatch, such as matching layers, become non-trivial because they are additionally required to facilitate a change in wave polarization. Acoustic and phononic metamaterials address this challenge by employing anisotropic unit cells that couple wave polarizations (Chen et al., 2014; Cao et al., 2021; Chai et al., 2023; Lee et al., 2024a; Liu et al., 2025). Mode conversion in metamaterials is typically achieved via two distinct mechanisms: one operating in the *long-wavelength* regime, and the other relying on *resonant* responses of the overall metamaterial or its mesoscale architecture.

The *long-wavelength* approach is used in the low-frequency domain where the wavelength greatly exceeds the characteristic unit cell size. In this regime, wave propagation can be accurately described by an effective elastic anisotropic medium, thereby enabling computationally efficient design approximations. Yang and Kim (2018a) derived the conditions for mode conversion between dissimilar isotropic materials using a quarter-wave impedance matching strategy, where conversion occurs at discrete frequencies determined by the matching plate length and material properties. Chen and Hu (2019) designed graded pentamode metamaterials to convert underwater cylindrical waves into planar fronts by rectifying the local transmission phase. Similarly, Lee et al. (2024b) designed a polarization-independent metasurface that achieves complete transmission and mode conversion at arbitrary refraction angles by introducing controlled phase shifts engineered with the unit cell geometry. Ahn et al. (2017) achieved parallel translation of longitudinal and shear waves via conical refraction and transducer phase tuning. See Jiang et al. (2014); Cao et al. (2021); Lin et al. (2021); Lee et al. (2022); He et al. (2023) for more examples.

Resonance-based designs rely on the dynamic response of metamaterials or their mesoscale architecture, but the resulting mode conversion is limited to narrow frequency bands dictated by resonant conditions. Wallen and Boechler (2017) studied shear-to-longitudinal mode conversion via second harmonic generation in two-dimensional hexagonally close-packed granular crystals. Similarly, Yi et al. (2023) investigated higher harmonic generation in dispersive metamaterial systems to facilitate mode conversion. Yang and Kim (2018b) applied topology optimization to design structures that support longitudinal-transverse mode conversion at interference-driven frequencies. Lee et al. (2024b) demonstrated shear circularly polarized wave transmission using Fabry–Perot interference, where optimal performance arises when the layer thickness is approximately one-quarter of the wavelength. In all these examples, the design dimensions and the topology are tuned to resonance (or interference) specific frequencies, which inherently constrain their operating bandwidth.

Functionally graded metamaterials (or gradient index metamaterials) allow gradual spatial variation in material properties, facilitating more continuous impedance transitions and reducing sensitivity to discrete resonant or geometric constraints (Smith et al., 2005; Jin et al., 2019; Chaplain et al., 2020). For example, in optical systems,

gradient-index designs have enabled effects such as broadband asymmetric waveguiding (Xu et al., 2013) and wave focusing (Jin et al., 2019). In mechanics and acoustics, such designs have enabled cylindrical-to-planar wave conversion (Chen and Hu, 2019), energy localization (Zelhofer and Kochmann, 2017), non-resonant mode separation (Zheng et al., 2020), low-pass elastic waveguides (Dorn and Kochmann, 2022, 2023), and Rayleigh wave redirection (Colombi et al., 2017). These gradient designs primarily address mode conversion within a single elastic medium, with limited attention to mode conversion across dissimilar materials. The role of graded metamaterials in mitigating polarization mismatch and enabling mode conversion across elastically dissimilar media, therefore, remains largely unexamined. In this work, we employ two-dimensional functionally graded metamaterials that use anisotropic unit cell shape variation to achieve longitudinal–shear wave conversion between isotropic media with large stiffness contrast. We discuss how key design parameters such as operating frequency, material properties, geometric scale, and unit cell designs influence the degree of conversion.

2. Design of the functionally graded metamaterial specimen

2.1. Design methodology

The objective of this work is to investigate the mechanism of longitudinal–shear wave mode conversion between two isotropic media with distinct elastic material properties (one stiff, one soft material). This is achieved through the use of a functionally graded anisotropic metamaterial (FGM) sandwiched between them as shown in Fig. 1. We begin by examining the scenario in which two semi-infinite, isotropic linear elastic media with differing elastic properties, denoted by Young’s modulus E , density ρ , and Poisson’s ratio ν , are joined at a sharp interface as illustrated in Fig. 1A. To facilitate experimental validation, we selected VeroWhite for the stiff material (shown in gray), with properties $E_{\text{VW}} = 2\text{GPa}$, $\rho_{\text{VW}} = 1190\frac{\text{kg}}{\text{m}^3}$, $\nu_{\text{VW}} = 0.35$, and TangoBlack for the soft material (shown in black), with properties $E_{\text{TB}} = 0.001\text{GPa}$, $\rho_{\text{TB}} = 1110\frac{\text{kg}}{\text{m}^3}$, $\nu = 0.49$.¹

When a harmonic longitudinal wave propagates from the stiff material through this system, the stark contrast in material properties causes significant reflection at the interface (Achenbach, 1999). The key factor governing wave transmission is the acoustic impedance (Z). For isotropic materials, longitudinal impedance is given by a scalar parameter $Z_L = \rho V_L$, where V_L denotes the plane stress longitudinal elastic wave speed. When the waves are traveling from a medium with impedance (Z_1) to a medium with impedance (Z_2), the ratio of reflected to total energy is given by $\frac{(Z_1 - Z_2)^2}{(Z_1 + Z_2)^2}$. For the present material combination, with $\frac{Z_{\text{VW}}}{Z_{\text{TB}}} \approx 40$, the incident wave is predominantly reflected with no mode conversion in the transmitted wave. This behavior is also evident in the transmitted horizontal velocity contours (V_1) shown in Fig. 1A. In contrast, impedance mismatch in anisotropic media results not only from variations in material density and wave speeds but also from differences in the modes of vibration (or polarization) as they exhibit directional dependent wave propagation and coupling between deformation modes. Moreover, the anisotropic acoustic

¹Both materials are commercially available and compatible with multi-material 3D printers such as Stratasys PolyJet.

impedance is represented by a tensor (Jiang et al., 2025), rendering impedance matching for mode conversion a non-trivial task.

Here, we employ a functionally graded anisotropic metamaterial as an interface between stiff and soft materials to achieve effective mode conversion. By gradually transitioning the unit cells from symmetric to asymmetric, the design enables a continuous gradation of effective material properties and a smooth evolution of deformation modes from uncoupled to strongly coupled, thus enhancing impedance matching. This behavior is also depicted in the transmitted horizontal velocity contours (V_1) shown in Fig. 1B. Our functionally graded metamaterial comprises unit cells organized into two distinct regions as shown in Fig. 1C. The central region contains shape gradients at constant density—referred to as density-preserving shape gradients. This region enables a gradual evolution of the mode shape and coupling while keeping the phase velocity nearly unchanged. The left and the right regions contain unit cells with similar patterns but with varying density, termed shape-preserving density gradients. These shape-preserving density gradients are aimed at maintaining the mode shape while gradually reducing the wave speed.

The dimensions and the number of unit cells are selected based on practical constraints associated with experimental fabrication and validation. In the central region, we place 13 unit cells to realize density-preserving shape gradients at a fill fraction of 0.65. We use a total of 14 square unit cells, seven at each end, to implement shape-preserving density gradients. Our graded designs vary only along the propagation direction, with the transverse axis held constant at 7 unit cells. The dimensions of the unit cells are 7.5×7.5 mm along each edge. With a total of 27 unit cells, the dimensions of the functionally graded design domain are $202.5 \times 52.5 \times 12$ mm.

2.2. Selection of unit cells in the functionally graded domain

The selection of a symmetric/asymmetric unit cell pair is central to our graded design. To pick unit cells, we utilize a pre-computed database from our previous work Boddapati and Daraio (2024). Multiple unit cells are suitable candidates, with each unit cell exhibiting distinct frequency-dependent dispersion behavior. In the low-frequency domain, wave propagation speeds are governed by the stiffness parameters C_{11}, C_{16}, C_{66} , where C_{11} is the axial stiffness, C_{66} is the shear stiffness and C_{16} is the shear-normal coupling stiffness (see Christoffel equations in Achenbach (1999)). Because asymmetric unit cells exhibit a non-zero shear-normal coupling C_{16} , we selected unit cells for the functionally graded metamaterial based on the extremal values of their elastic tensor components. For the symmetric unit cell, we pick a geometry that exhibit a very high C_{11} among all the unit cells with a 0.65 fill fraction. This corresponds to unit cell 8 in Fig. 1C. Similarly, for the asymmetric unit cell, we selected a geometry with a high C_{16} at the fill fraction 0.65, such that $C_{16} > C_{66}$. This corresponds to unit cell 20 in Fig. 1C. The static homogenized properties of the symmetric and asymmetric unit cells in the vectorized format are $[617.83, 213.06, 617.83, 0.00, 0.00, 170.04]^T$ MPa, $[215.03, 87.18, 98.21, 90.66, 66.91, 78.16]^T$ MPa, respectively ².

Static stiffness parameters alone cannot fully describe dynamic wave behavior, as unit cells with similar static properties can exhibit different dynamic responses. However, they serve as a valuable first-order approximation for

²In the vectorized format, the stiffness components are ordered as $[C_{11}, C_{12}, C_{22}, C_{16}, C_{26}, C_{66}]^T$.

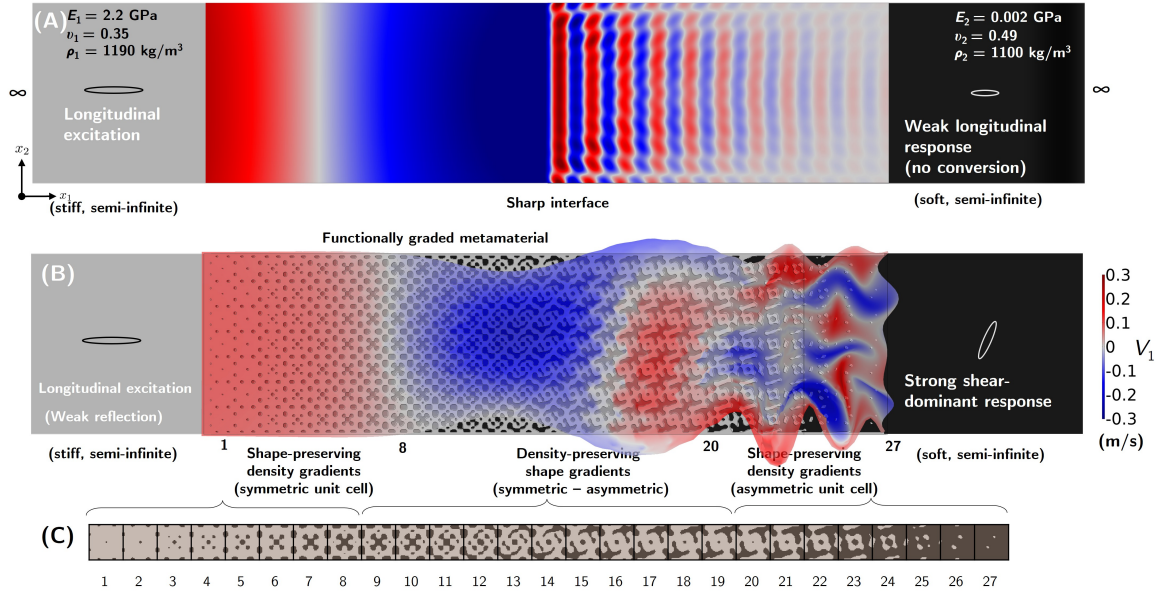


Figure 1: (A) A semi-infinite medium made of two isotropic materials with a sharp interface between a stiff and soft material. At steady state, a longitudinal periodic excitation (at the left) results in only a smaller amplitude longitudinal response (at the right) due to impedance mismatch. (B) A functionally graded design is sandwiched between two isotropic materials in the semi-infinite medium. The graded design enhances conversion by coupling deformation modes. The shape gradients in unit cells (8 to 20) allow the wave mode to convert from longitudinal to a hybrid shear-dominant mode. The density gradients in unit cells (1 to 8 and 20 to 27) help gradually reduce the wave speed while retaining the mode shape. (C) Unit cells in the graded design domain numbered from the left end to the right end.

preliminary design assessments. We evaluated a total of 30 designs by sampling different unit cell pairs; following an initial first order analysis, this specific pair was selected for detailed frequency-domain analysis. To interpolate between unit cells and obtain a graded design, we adopt the approach introduced in our previous work [Boddapati and Daraio \(2024\)](#). The procedure involves defining the unit cell shape by applying a binary threshold to a function constructed as a sum of cosine functions. Spatial variation in unit cell geometry is achieved by modulating the coefficients of this cosine-based function.

2.3. Dispersion analysis of the unit cells in the graded domain

Due to the discrete and structured nature of the unit cells, wave propagation behavior depends on the frequency of excitation. Consequently, the impedance of each unit cell (and the whole structure³) becomes frequency-dependent. Thus, dispersion analysis of individual unit cells informs the selection of an appropriate frequency range for mode conversion analysis. The frequency-dependent dispersion behavior of the unit cells is analyzed using an in-house numerical homogenization finite element code ([Ogren et al., 2024](#)). Each unit cell is modeled as a 50×50 bilinear mesh with each element taking either stiff or soft phase.

³Using a different interpretation, it is possible to consider this whole region as a single block and obtain a homogenized impedance.

In Fig. 2A, the dispersion band diagrams are plotted for the waves propagating along x_1 direction for the first two modes. The mode with the lowest eigenvalue is termed as a shear dominant mode, while the mode with the second eigenvalue is termed as a longitudinal dominant mode. Notably, the dispersion curves for both modes exhibit a downward shift from left to right across the graded unit cells. This trend indicates a progressive reduction in wave speed for a given excitation frequency as the wave traverses from the left to the right unit cells. At low frequencies, wave propagation is primarily influenced by the stiffness contrast between the two phases. As the frequency increases, however, density differences begin to play a more dominant role. For the Verowhite–Tangoblack material combination considered here, the density contrast is minimal while the stiffness contrast is high. As a result, the dispersion relation exhibits flat bands at higher frequencies—a feature that also appears in modes beyond the first two.

The evolution of mode shapes of a subset of unit cells is also plotted in Figs. 2(B-C) at a fixed wavenumber $\gamma = 0.167\frac{\pi}{a}$ with contour representing horizontal displacements in both cases, where a is the size of the unit cell. For the unit cell at the left boundary with shape-preserving density gradients (index = 1 to 7), the first mode is a pure shear mode, and the second mode is a pure longitudinal mode. Both modes show hybridization between longitudinal and shear modes for the unit cells in the central region (index = 7 to 20), with enhanced coupling witnessed by the deformation mode in unit cells 18 to 22. The fill fraction variation is shown in the right inset of Fig. 2D, which further illustrates the shape and the density gradients described in Fig. 1C. Dispersion band diagrams for all the unit cells are plotted in Figs. 2(E-F). Overall, the analysis from mode shapes and dispersion band diagrams indicates a gradation in wave velocities and polarization (and thus impedance) that is required for mode conversion. Based on this analysis, a frequency range of 1–10 kHz is selected for investigating mode conversion, as highlighted in Figs. 2(E-F).

3. Results and discussion

3.1. Comparison of designs using numerical data for longitudinal-to-shear conversion

To assess the effectiveness of the graded design in facilitating mode conversion across the selected frequency range, we numerically investigate three different designs shown in Fig. 3. The design in Fig. 3(A), named *symmetric design*, is entirely made of the symmetric unit cell, while the design in Fig. 3(B), named *asymmetric design*, is entirely made up of the asymmetric unit cell. The design in Fig. 3(C) is the functionally *graded design* with the shape and the density gradients between the symmetric and asymmetric unit cells as discussed in Section 2. On the left boundary, we apply a harmonic excitation by prescribing a horizontal velocity ($V_1 = 0.1$ m/s, $V_2 = 0.0$ m/s), while the right end is modeled with a perfectly matched layer. The frequency is changed from 1000 Hz to 10000 Hz in steps of 250 Hz. A detailed explanation of the numerical modeling framework, including the boundary conditions and the locations of input and output signal measurements, is provided in Section 4.1 and also illustrated in Fig. A.9.

To quantify the mode conversion, the horizontal (V_1) and the vertical velocity (V_2) components cannot be used directly to quantify mode conversion, as they are coupled due to non-zero Poisson’s ratio. Therefore, the degree of mode conversion is quantified by evaluating the ellipticity of particle trajectories at each point, analogous to the

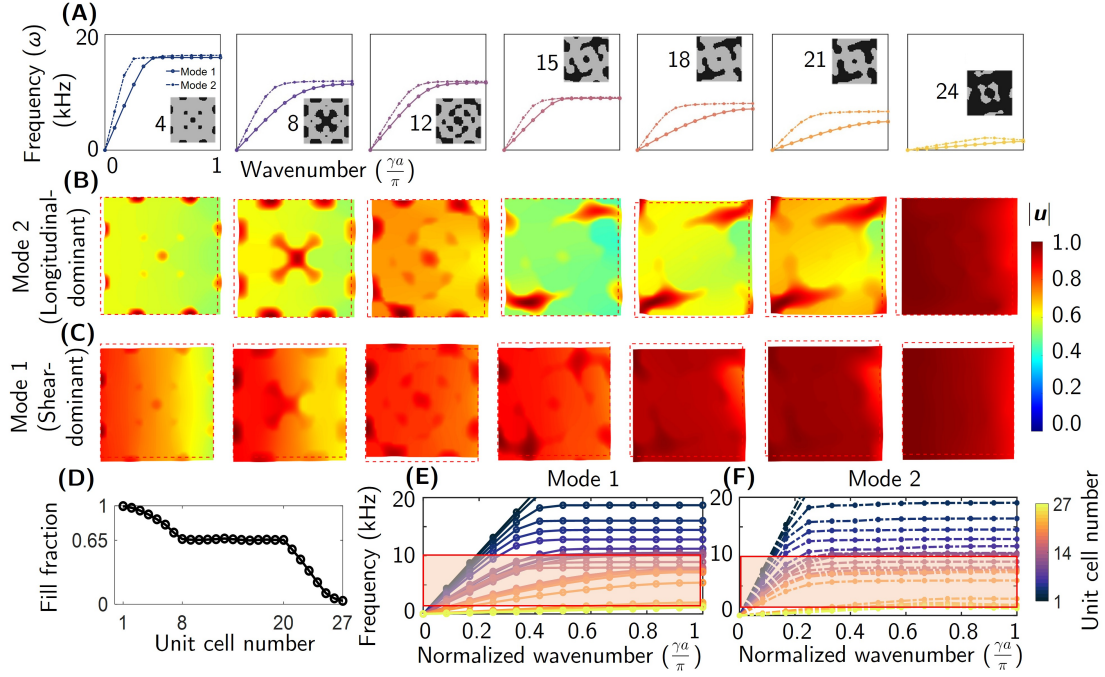


Figure 2: (A) Dispersion band diagram for waves propagating along x_1 axis (Normalized wavenumber $(\frac{\gamma^a}{\pi})$ – frequency (ω) plots). Only, the first two modes of a subset of unit cells are shown. The first mode is purely shear, and the second mode is purely longitudinal for the unit cell 1. Rest of the unit cells exhibit mode hybridization. (B-C) Mode shapes of the same subset of unit cells are plotted at a fixed wavenumber $\gamma = 0.167\frac{\pi}{a}$. The color contour shows normalized values of displacement magnitude. (D) Plot of the fill fraction of the stiff material with unit cell number, showing density gradients between unit cells 1 to 8 and 20 to 27. (E-F) Overly of dispersion band diagrams for all the unit cells in the functionally graded structure for modes 1 and 2 respectively.

approach used for Rayleigh wave ellipticity (Achenbach, 1999). If θ is the orientation of the major axis of an ellipse relative to the x_1 direction, then the polarization is given by $|\cos(\theta)|$. When the major axis of the resulting ellipse aligns along the x_1 direction, the motion is classified as purely longitudinal (polarization = 1). Similarly, alignment of the major axis along the x_2 direction indicates a pure shear motion (polarization = 0). For cases where the major axis is oriented at an intermediate angle between x_1 and x_2 directions, the motion is hybridized (see Fig. A.10). Further, the signal amplitude, expressed as $\frac{\sqrt{V_1^2 + V_2^2}}{V_p}$, is defined as the magnitude of the velocity vector normalized with the prescribed velocity V_p . To capture the distribution of amplitude and polarization values in the output region, violin plots are employed (Hintze and Nelson, 1998). The width of the violin plot represents the kernel density distribution (the number of points at that particular value) of the data, and the black dots denote the median values.

Mode conversion is interpreted through both deformation mode shapes and violin plot distributions. In Figs. 3(A-C), the computed horizontal velocity component (V_1) at three different frequencies (2000 Hz, 4000 Hz, 8000 Hz) is shown. The variation of the velocity signal amplitude measured at the output region, as detailed in Fig. A.9, is plotted on a log scale in Figs. 3(D-F). Similarly, the variation of polarization as a function of excitation frequency

is plotted in Figs. 3(G-I). For all designs, the boundary conditions enforce a unit amplitude and polarization of the input signal. The signal amplitude at the output may exceed 1 due to coupling between the V_1 and V_2 components arising from the nonzero Poisson's ratio. For the graded design, the transmitted signal drops by nearly two orders of magnitude as the frequency increases, with a pronounced attenuation beyond 7 kHz due to damping and the presence of flat bands in the dispersion characteristics of the unit cells near the right end. Unlike the graded design, the symmetric and asymmetric designs exhibit only mild attenuation, with the signal amplitude decreasing by less than an order of magnitude over the entire frequency range. For all designs, the structural deformation at low frequencies is predominantly longitudinal, as governed by effective continuum behavior, with polarization values close to 1. As the frequency increases, the dispersive behavior of the unit cells induces mode conversion, which is more pronounced in the 2000 Hz – 6000 Hz range, with polarization values less than 0.7 for asymmetric and graded designs. Beyond 8000 Hz, minimal mode conversion is observed. Overall, the graded design shows significant conversion in amplitude as well as polarization in comparison to the asymmetric design between 2750 Hz - 4750 Hz, as also seen in the particle trajectories in Fig. A.10. Further, the graded design also displayed a strong shear-to-longitudinal conversion at 4000 Hz relative to the asymmetric and symmetric designs, as shown in Fig. 4. Please refer to the animations attached in the supplementary information extracted at 4000 Hz, which reveal dynamic features not evident in the static plots.

3.2. Comparison of experimental data with numerical simulations for graded design

We experimentally validate the longitudinal-to-shear mode conversion in the graded design by measuring full-field velocity data using laser Doppler velocimetry (LDV) on an additively manufactured specimen. The experimental setup and data acquisition are explained in detail in Section 4.2 and Section 4.3, respectively. The specimen is excited using a chirp signal to capture the response at all frequencies in the range of interest. The particle velocity at each sampling point measured using LDV in the time domain is converted to the frequency domain using the Fourier transform. The magnitudes of the velocity fields (V_1, V_2) across the whole domain are plotted at selected frequencies in Fig. 5. These frequencies are selected to be non-uniformly spaced to emphasize regions exhibiting peak conversion behavior. Between 3200 - 5600 Hz, the mode shapes look asymmetrical indicating a strong conversion in this frequency range. Beyond 5600 Hz and frequencies below 2400, the mode shapes look symmetric, and minimal conversion is noted. Please refer to the animations provided in the supplementary information. The first animation Full_Bandwidth_1000Hz_10000Hz.mp4 illustrates mode conversion using a chirp signal spanning the full 1–10 kHz spectrum, while the second animation Narrow_Bandwidth_3.8kHz_4.2kHz.mp4 focuses on a narrow bandwidth (3800–4200 Hz) where the deformation is observed to be shear-dominant.

In addition, the magnitudes of the horizontal and vertical velocity components measured near the shaker tip, the input, and the output region are shown in Fig. A.8. The measured shaker input is almost purely longitudinal, as seen with a low V_2 component, except near the frequencies where mode conversion is observed. Further, the signal measured near the shaker tip is comparable to the signal measured near the graded design input, indicating minimal loss until the onset of the graded design. However, the shaker input is not temporally uniform, although the

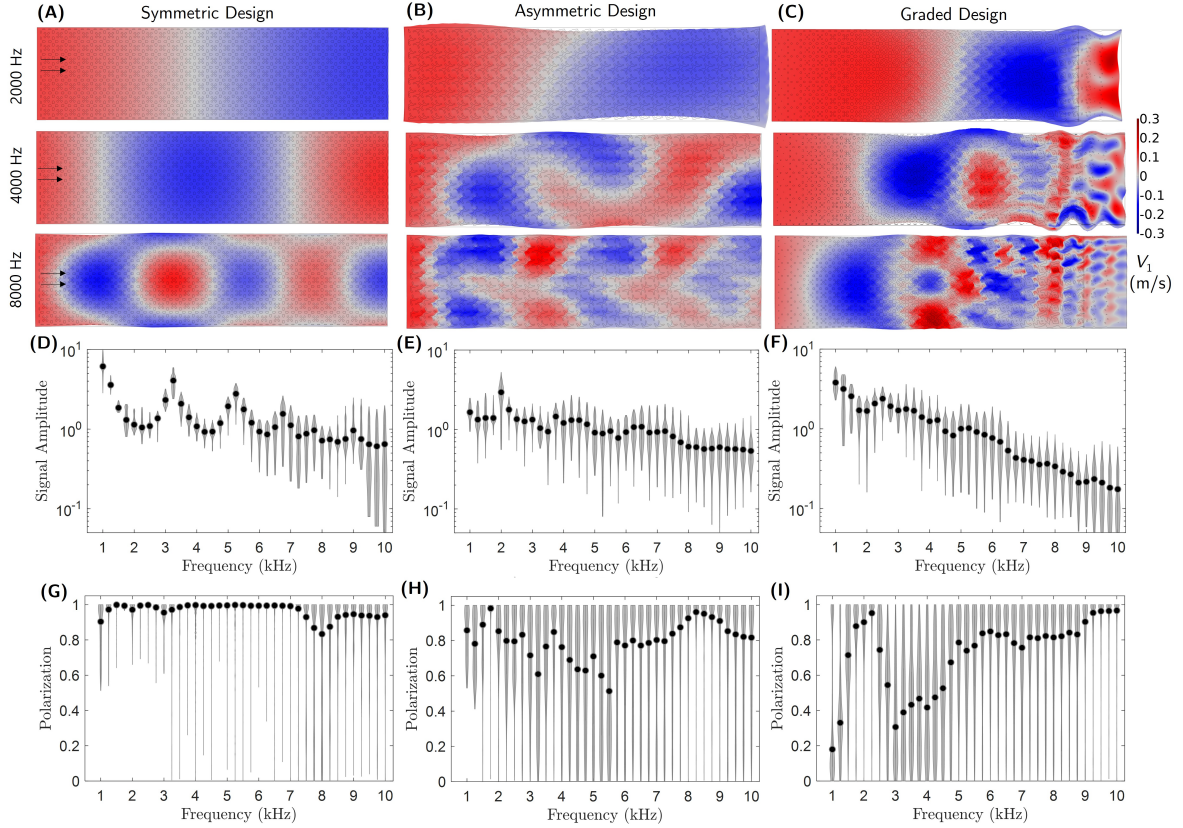


Figure 3: Comparison of transmission spectrum for three designs under longitudinal excitation. (A-C) Contours of horizontal velocity component V_1 for symmetric, asymmetric, and graded designs at three different frequencies (2000 Hz, 4000 Hz, 8000 Hz). (D-F) Plots of the variation of the transmitted signal evaluated at the output with the frequency of excitation (normalized with the input). (G-I) Plots of the variation of the polarization evaluated at the output with the frequency of excitation.

chirp signal is designed to provide uniform input, which could be attributed to the frequency-dependent structural impedance of the overall setup. Consequently, normalizing the output data by the input signal for comparison with numerical simulations becomes non-trivial. The signal measured near the graded design output drops further with frequency, especially beyond 7 kHz, consistent with numerical observations. The output shows an overall stronger signal in both V_1 and V_2 components between 3.5 - 5.5 kHz range, which also corresponds to the frequency range where the mode shapes indicate maximum conversion.

Overall, the experimental results qualitatively align with trends observed in the numerical simulations. However, a direct one-to-one comparison is not feasible due to differences in the experiments to simulations: from the excitation setup as well as the material modeling. Specifically, the shaker with a point-like source was positioned relatively far from the functionally graded structure, which limited the generation of a pure plane wave at the onset of the graded region. Further, in contrast to the numerically predicted small-wavelength deformations concentrated in the softer region, the experiments displayed hybridized deformation of the entire structure, highlighting modeling limitations

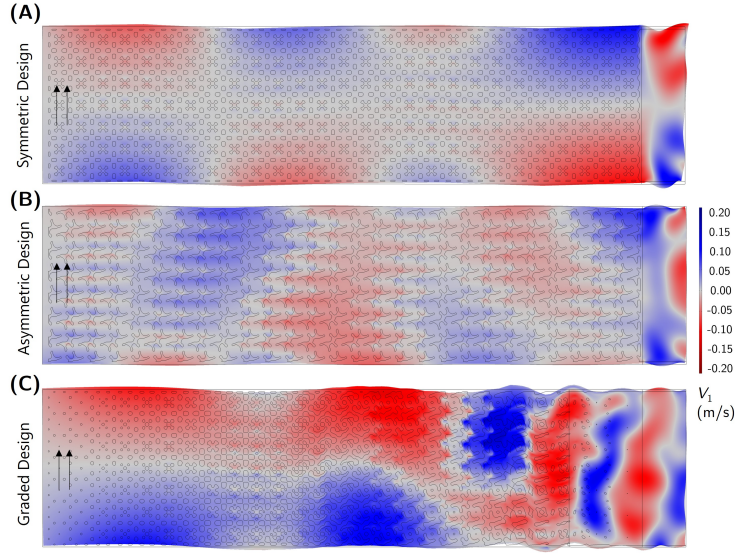


Figure 4: Comparison of deformation shapes for the three designs under shear excitation at 4000 Hz, showing a mixed deformation mode in the softer region of the graded design. Contours display the horizontal velocity component (V_1).

of such a highly heterogeneous system. In other words, in the frequency range where we observed a stronger mode conversion in experiments, the overall deformation mode exhibited a shear-like characteristic, with both input and output regions not in pure longitudinal mode.

Both VeroWhite and TangoBlack are polymer-like materials exhibiting intrinsic viscoelastic damping and frequency-dependent elastic behavior (Zorzetto et al., 2020), while the simulations adopt frequency-independent linear elastic material parameters to simplify modeling complexity. We chose these materials for their compatibility with additive manufacturing, which made specimen preparation and testing more straightforward. Incorporating viscoelastic and hyperelastic effects into the material models would allow for a more accurate representation of experimental conditions and inform metamaterial design strategies. However, such sophisticated modeling approaches are beyond the scope of the present study.

3.3. Hyperparameter effects

Using non-dimensional analysis, the frequency dependence on the material and geometric parameters can be given as $\omega \propto \frac{1}{L} \sqrt{\frac{E}{\rho}}$. This relation implies that reducing the unit cell dimensions shifts the mode-converting behavior into the high-frequency domain (> 20 kHz), enabling applicability in ultrasound regimes (Gerard et al., 2019). Likewise, for a fixed scale of the unit cell, when the elastic modulus of the constituent materials is increased, a comparable deformation is observed at higher frequencies. The graded design domain's total length and width of the specimen are also hyperparameters that influence mode conversion. When the graded domain overall length was reduced to half of its original value by reducing the number of unit cells, both numerical and experimental results showed significantly

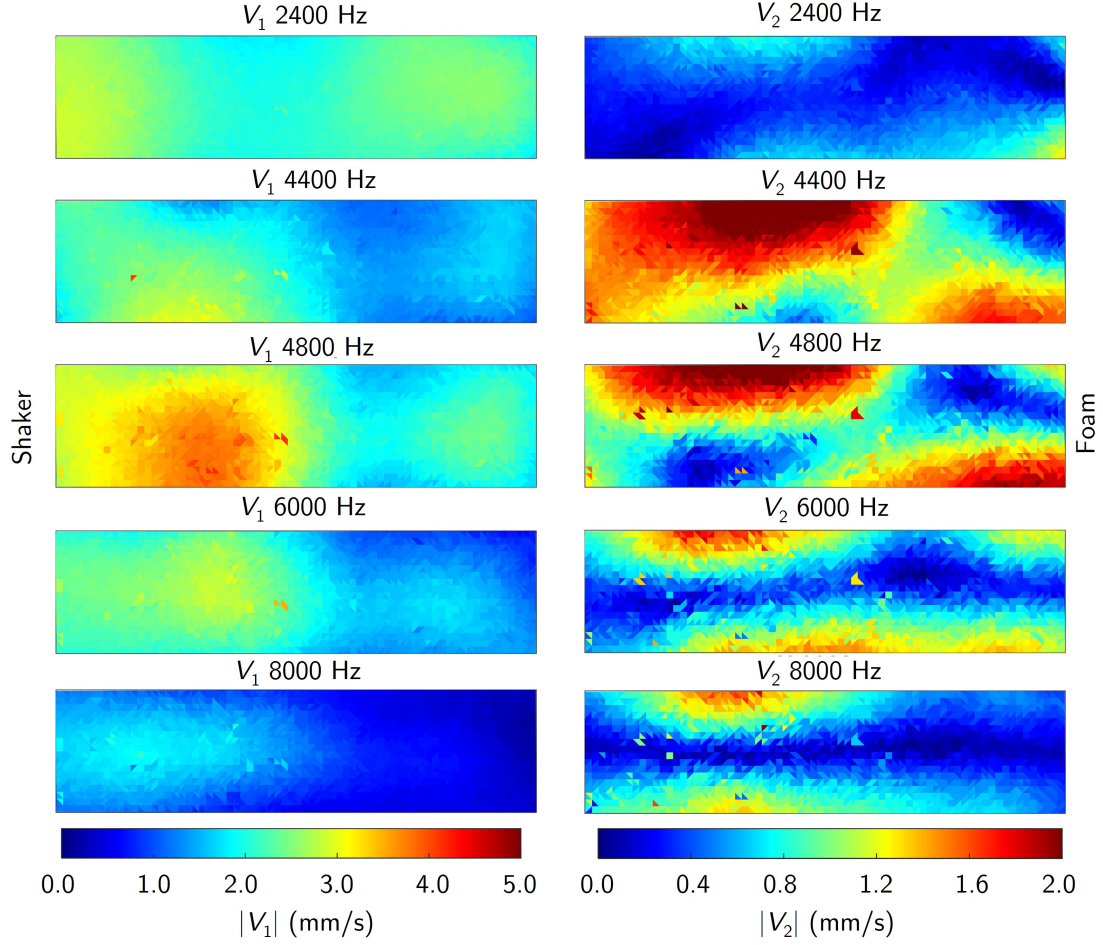


Figure 5: Plot of magnitude of velocity components at selected frequencies, measured experimentally. Mode shapes are symmetric at frequencies near 2400 Hz and 8000 Hz, indicating no conversion. Mode shapes are asymmetric near 4400 Hz, indicating a shear deformation mode for longitudinal excitation.

diminished conversion performance. Overall, these findings underscore that achieving efficient mode conversion requires not only tuning unit-cell parameters but also accounting for the total length and width of the design domain.

To design structures for the desired dynamic response, we relied on the static properties as a design guide. Therefore, our design approach focused on the broadband hybridized conversion over perfect conversion at a specific frequency. To enhance mode conversion at a particular frequency, topology optimization can be employed to design compact structures with high conversion efficiency, as demonstrated in previous studies (Lin et al., 2021; Kim et al., 2023; Jiang et al., 2025). Impedance gradation obtained by simultaneously varying density and geometric parameters could serve as the objective function for such optimization problems. Furthermore, incorporating more than two constituent materials in the design domain, such as localized inclusions of a very high-density material, could greatly broaden the design space and allow stiffness and density to be tuned independently.

3.4. Design of a radial transducer based on mode-converting graded structures

Novel transducers and actuators utilizing mode conversion enable applications in directional sound propagation (Jiang et al., 2014; Guo, 2025), wearable devices (Dal Poggetto et al., 2023), and acoustic tweezers (Yang et al., 2025). In this section, we explore graded metamaterial in a circular domain to facilitate conversion between radial and tangential wave modes. Specifically, the shape gradient region of the graded structure with unit cells from 8 to 20 (shown in Fig. 1C) is conformally mapped onto an annular disc, featuring symmetric unit cells near the inner edge and asymmetric unit cells at the outer edge (see Fig. 6A, Fig. 6C). For this configuration, we consider two independent excitation scenarios at the inner circular boundary: (i) radial excitation, and (ii) tangential excitation with a perfectly matched boundary condition maintained at the outer edge. Radial excitation may be introduced via a piezoelectric transducer or pressurized gas/fluid, while tangential excitation can be provided using a motor-driven mechanism (Wang et al., 2021).

The annular disc has an inner diameter of 4 mm and an outer diameter of 40 mm, comprising of $N_c = 56$ unit cells along the circumferential direction and $N_r = 14$ unit cells along the radial direction. The size of the unit cells at any radial location R is given by $\frac{2\pi R}{N_c}$. As a result, the unit cells in the inner edge are of size 0.44 mm while the unit cells at the outer edge are of the size 4.4 mm. Furthermore, the aspect ratio of the unit cells also changes from the inner edge to the outer edge, with unit cells at the outer edge being wider in the circumferential direction. At $R = 10$ mm, the unit cells are approximately square in aspect ratio and one-third in size compared to those shown in Fig. 3. Therefore, utilizing the scaling analysis mentioned in Section 3.3, we study the frequency response of this design in 1-20 kHz range.

We examine the design's capability to convert radial excitation at the inner boundary into a tangentially dominated response at the outer boundary, and vice versa. Radial velocity is defined as $V_{\text{Radial}} = \mathbf{V} \cdot \mathbf{n}$, where \mathbf{n} is the outward normal vector. Similarly, tangential velocity is defined as $V_{\text{Tangent}} = \mathbf{V} \cdot \mathbf{t}$, where \mathbf{t} is the counter-clockwise tangent vector, with $\mathbf{n} \cdot \mathbf{t} = 0$. In Figs. 6(A-B), we show the radial and the tangential velocity components under radial excitation at 10 kHz, where the tangential component is higher than the radial component and marked with x in Fig. 6E. We observe that at low frequencies, the response is that of a continuum and purely radial, similar to linear designs as seen in Section 3.1. As the frequency increases, the deformation is hybridized and tangentially dominated with velocity contours showing directionality, with peak conversion in the 6–12 kHz range. Similarly, Figs. 6(C-D) illustrate the velocity components under tangential excitation at 15 kHz, where the radial component is higher than the tangential component, marked with x in Fig. 6F. Overall for this design, the conversion from the radial-to-tangential mode is high compared to the tangential-to-radial mode. In future studies, the unit cell design and conformal mapping parameters can be further tuned to enhance conversion efficiency.

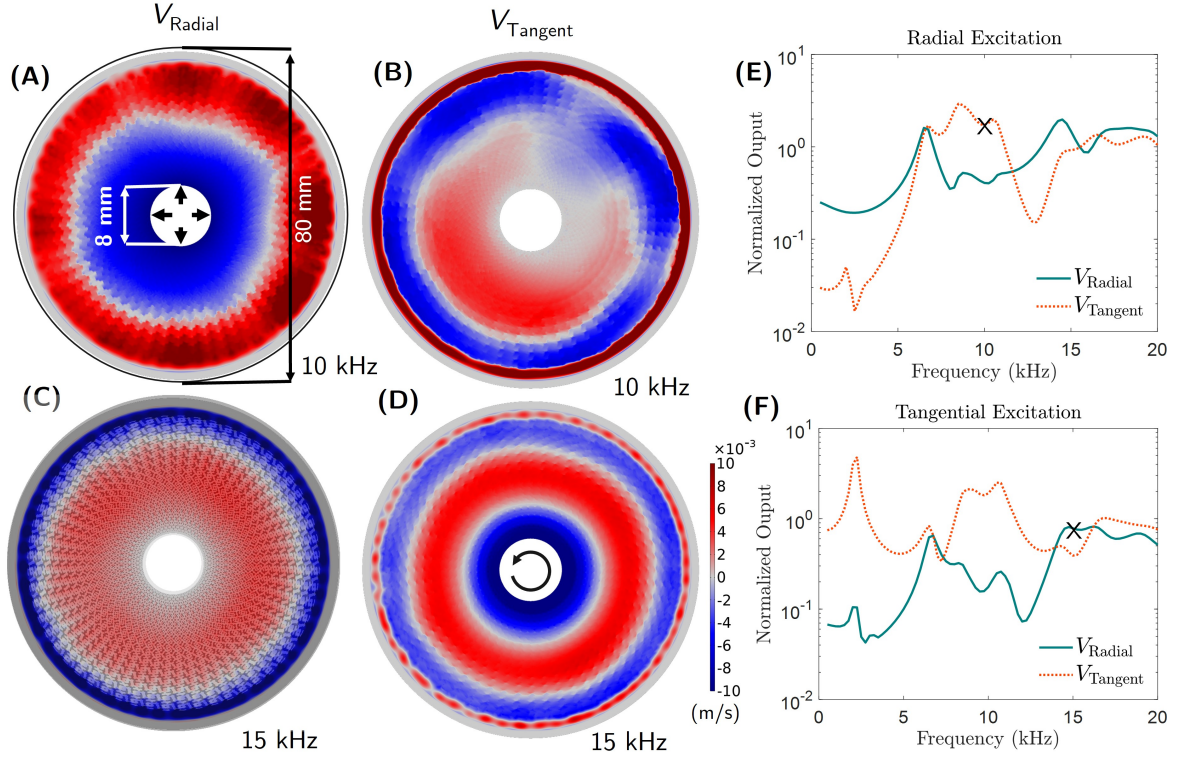


Figure 6: Radial-tangential mode conversion for transducer applications. (A, B) Radial and tangential velocity components under radial excitation at 10 kHz. (C, D) Radial and tangential velocity components under tangential excitation at 15 kHz. (E, F) Variation of absolute velocities averaged at the output. The x-mark indicates the point chosen for contour plots where conversion is higher.

4. Methods

4.1. Numerical simulations

The steady-state, frequency-dependent response of the structures is examined using COMSOL's frequency domain analysis. On the left boundary, a harmonic excitation is provided in the form of a prescribed velocity, which results in a plane wave $\mathbf{u}(\mathbf{x}, t) = u_p \exp(i\omega t)$, where ω is the frequency of excitation, i is the complex number, $p \in [1, 2]$. When $p = 1$, the excitation is longitudinal, while $p = 2$ is a shear excitation. To enable wave transmission while minimizing reflections, the right boundary of the domain is modeled as a *perfectly matched layer* (PML). Quadratic serendipity elements are employed with a fine mesh, ensuring that the element size is significantly smaller than the observed wavelengths. See Fig. A.9 for more details on boundary conditions and the mesh. In the steady state, a plane-stress solution of the form $\mathbf{u}(\mathbf{x}, t) = \mathbf{u}(\mathbf{x}) \exp(i(\omega t - \phi))$ is considered, where ϕ is the phase difference relative to the excitation. The storage modulus of TangoBlack (akin to other viscoelastic materials) generally increases with frequency (Zorzetto et al., 2020). Therefore, to account for the apparent frequency-dependent modulus of TangoBlack, we use $E = 10$ MPa in our COMSOL simulations, instead of its quasi-static modulus $E = 0.7$ MPa. Further, an

isotropic loss factor of 0.1 is applied to account for damping in both materials.

4.2. *Experimental setup and testing*

The testing specimen is fabricated using a commercial multi-material polyjet technology-based 3D printer, Stratasys Objet500 Connex. One end of the specimen is connected securely to the shaker (Brüel & Kjær's rectilinear mini-shaker type 4810) using a screw printed on the specimen (see Fig. 7). The shaker operates within the prescribed range of DC–18 kHz, aligning with our frequency range of interest. The other end of the specimen is embedded into a super-cushioning polyurethane foam (McMaster-Carr® 8643K547) to minimize reflections (emulating an infinite medium). The bottom surface of the specimen is lubricated and rests on a low-profile ball transfer plate (McMaster-Carr® 5764K32), which allows for near-frictionless planar movement. The ball transfer plate is further supported on four vibration-damping sandwich mounts (Global Industrial® WBB831528) to isolate vibrations from the base of the setup. Full-field velocity measurements are obtained using 3D laser doppler vibrometer (Polytec® PSV QTec 3D). The surface is coated with the commercially available retroreflective glass powder (Cospheric® P2453BTA) to enhance LDV's signal-to-noise ratio.

4.3. *Experimental data acquisition*

The specimen was excited using a 50 ms chirp signal spanning 1–11 kHz, generated in MATLAB. The signal was loaded into the built-in signal generator of the LDV system and then amplified by a power amplifier (Brüel & Kjær, type 2718) to drive the shaker with sufficient voltage. As the domain of interest is large, the whole domain is observed in a mirror to get a better signal-to-noise ratio from reflected laser light (see left inset in Fig. 7). The data is suitably converted from the mirror plane to the specimen plane utilizing coordinate frame transformation. We sample the region of interest with 19×71 equally spaced points, which translates to 6-7 measurement points per unit cell. Phase velocities at each measurement point were acquired at a 100 kHz sampling rate using LDV, ensuring approximately five times the Nyquist frequency for the frequency range of interest. The measurement at each point is averaged over 32 times to improve the signal-to-noise ratio. Once the particle velocity of each measurement point is acquired in the time domain, the data is converted into the frequency domain using the Fourier Transform (FFT) (see right inset in Fig. 7). The input near the shaker is measured separately, and the same procedure is followed to convert data into the frequency domain (see Fig. A.8).

5. **Conclusions**

In this work, we demonstrated the broadband longitudinal-to-shear mode conversion of planar waves between dissimilar materials using functionally graded structured materials. The graded design transitions from unit cells with no shear normal coupling to those with high shear normal coupling. This, in turn, helps reduce impedance mismatch due to polarization, as our results show that smooth geometric gradation induces a graded transition in dispersion behavior—from purely longitudinal mode to shear-dominant hybridized mode. At low frequencies, the

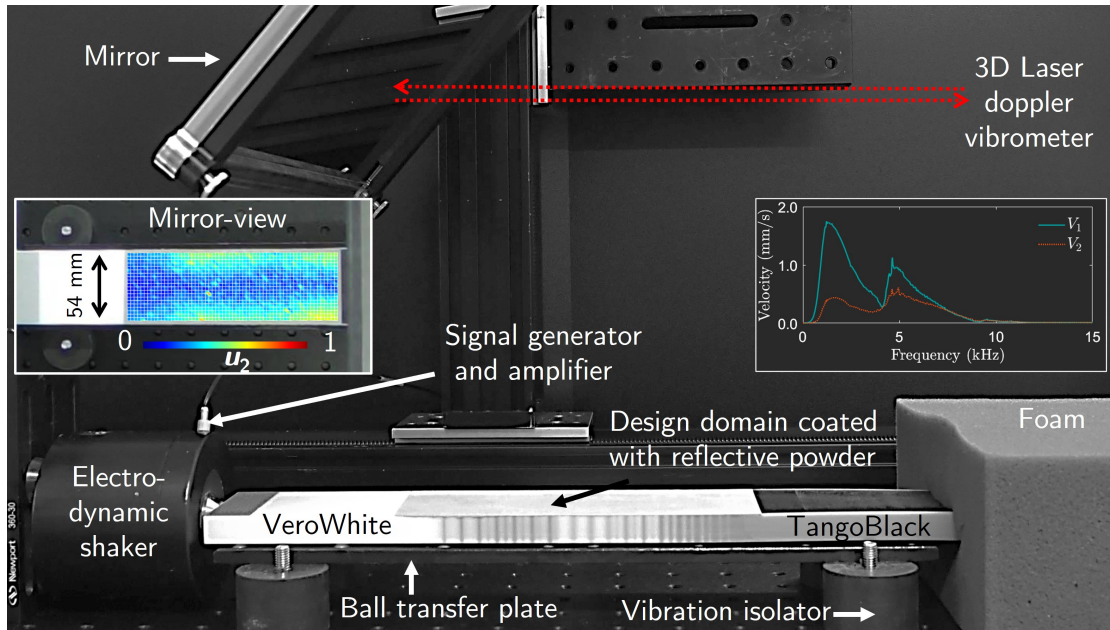


Figure 7: Additively manufactured specimen consists of the VeroWhite (stiff) and TangoBlack (soft) regions, sandwiched by a functionally graded metamaterial. The left end of the specimen is attached directly to a shaker, while the right end is embedded in a foam to minimize reflections, emulating an infinite domain. The electrodynamic shaker provides a longitudinal excitation using the signal received from the signal generator and amplifier. The whole length of the specimen rests on a ball-transfer plate that facilitates near-frictionless in-plane motion. The ball-transfer plate is supported on four vibration-isolating mounts. Full-field velocity measurements on the surface of the design domain are obtained using a three-dimensional laser Doppler vibrometer (LDV). The LDV tracks a grid of points on the specimen as reflected in the mirror (see inset image). The dimensions of the specimen are $322 \times 54 \times 12$ mm, including the portion that is attached to the shaker as well as the portion that is embedded in the foam.

structure behaves like an effective continuum, showing minimal mode conversion but strong signal transmission. At high frequencies, the response is dominated by unit-cell dispersion, leading to weaker transmission and conversion. At intermediate frequencies, the design exhibits high mode conversion and strong transmission. Full-field laser Doppler velocimetry measurements conducted on the additively manufactured specimen corroborate the observed numerical behavior, indicating a stronger conversion between 3500 Hz and 5500 Hz. The graded design was further implemented to enable conversion between radial and tangential wave modes, making it suitable for transducer applications.

In the future, unit cell designs with more than two constituent materials can be optimized to enhance mode conversion. Extending the design methodology into three dimensions facilitates the investigation of more intricate wave mode interactions, such as transitions between torsional–bending waves and Rayleigh–Lamb waves. By embedding stimuli-responsive materials, such as magnets, these structures can be tuned on demand and explored in nonlinear regimes, enabling applications in wearable sensing, transducer design, and soft robotics.

CRediT authorship contribution statement

Jagannadh Boddapati: Conceptualization, Methodology, Investigation, Formal analysis, Writing - original Draft. **Jihoon Ahn:** Conceptualization, Methodology, Investigation, Formal analysis, Writing - review and editing. **Alexander C. Ogren:** Conceptualization, Methodology, Software, Validation, Writing - review and editing. **Chiara Daraio:** Conceptualization, Methodology, Writing - review and editing, Supervision, Funding acquisition.

Acknowledgments and Code

The authors would like to thank Dr. Gunho Kim (Caltech) for helpful discussions on numerical simulations. The authors gratefully acknowledge financial support provided by the United States National Science Foundation under grant awards 2052827 (C2SHIP) and 2242925 (NEWFOS), as well as funding from the US Heritage Medical Research Institute under grant award HMRI-15-09-01.

The dispersion analysis code is available at <https://github.com/aco8ogren/2D-dispersion>.

Appendix A. Additional information

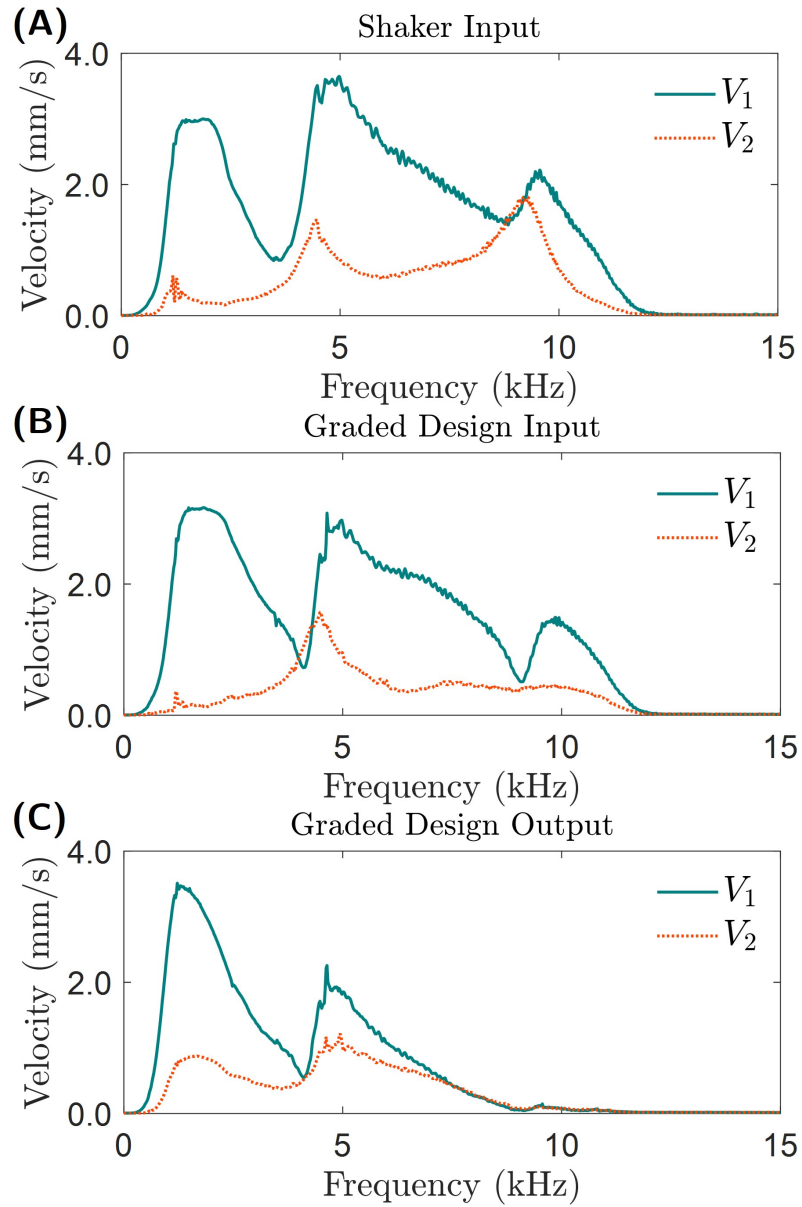


Figure A.8: Magnitude of velocities from LDV data. A) Input velocity components, averaged in absolute value near the shaker tip, showing the frequency-dependent behavior of the combined shaker–specimen system. The chirp signal results in a shaker input confined to 1–11 kHz. B) Velocities averaged near the start of the graded design. The data shows that the graded design’s input signal almost matches the signal measured near the shaker tip, indicating minimal transmission loss. C) Velocities averaged near the end of the graded design. This demonstrates signal attenuation arising from transmission losses, consistent with patterns observed in numerical simulations.

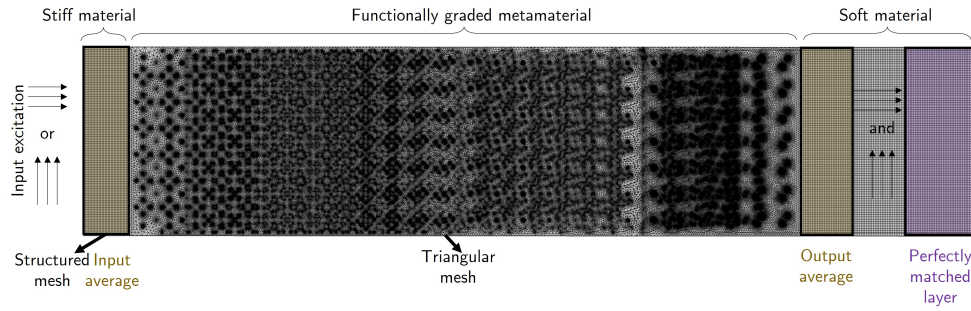


Figure A.9: Description of the boundary conditions and the mesh for numerical simulations. At the left boundary, input excitation is provided using *prescribed velocity* option in COMSOL. At the right boundary (marked in purple), a *perfectly matched layer* (PML) boundary condition is prescribed to allow waves to pass while minimizing reflections, following a setup similar to Lin et al. (2021). The PML is configured using polynomial coordinate stretching, with a scaling factor of 10 and a curvature scaling factor of 1. A triangular mesh with quadratic serendipity elements is used for the graded domain. A mapped structured mesh is used for the PML, as well as for the input and the output regions. The input is averaged over the shaded area left of the graded region (marked in yellow), while the output is measured in the shaded area right of the graded design (marked in yellow), mirroring the experimental measurement locations used to capture the input and the output responses.

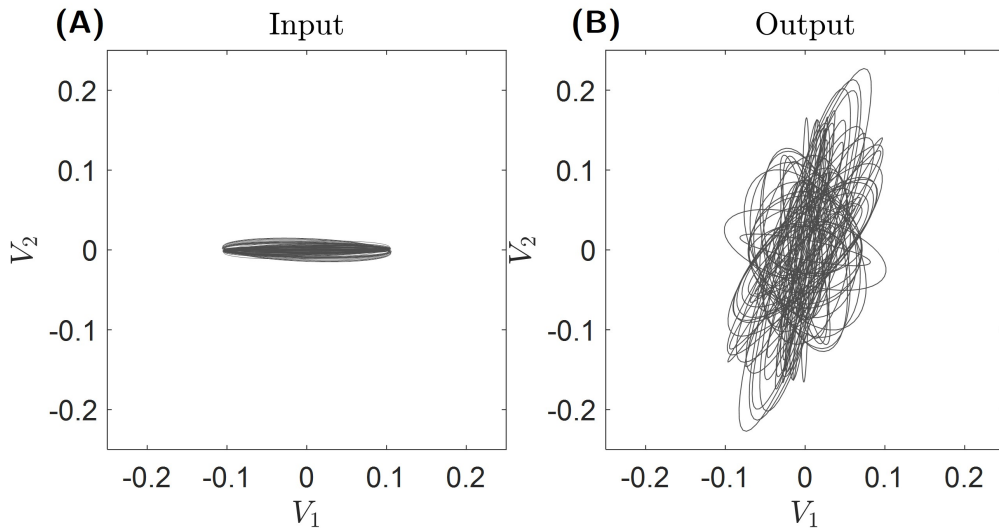


Figure A.10: A comparison of particle velocity trajectories from simulations at 4000 Hz under longitudinal excitation for the input and output regions of the graded design. (A) At the input, the major axes of the ellipses are oriented along x_1 for all nodes, as dictated by the boundary conditions. (B) At the output, the major axes of the ellipses are strongly aligned along x_2 for most of the nodes, indicating a strong mode conversion.

References

Achenbach, J.D., 1999. Wave propagation in elastic solids. Number 16 in North Holland series in applied mathematics and mechanics. 1. paperback ed., 8. impr ed., North-Holland, Amsterdam.

- Ahn, Y.K., Lee, H.J., Kim, Y.Y., 2017. Conical Refraction of Elastic Waves by Anisotropic Metamaterials and Application for Parallel Translation of Elastic Waves. *Scientific Reports* 7, 10072. URL: <http://www.nature.com/articles/s41598-017-10691-6>, doi:10.1038/s41598-017-10691-6.
- Boddapati, J., Daraio, C., 2024. Planar structured materials with extreme elastic anisotropy. *Materials & Design* 246, 113348. URL: <https://www.sciencedirect.com/science/article/pii/S0264127524007238>, doi:10.1016/j.matdes.2024.113348.
- Cao, L., Zhu, Y., Xu, Y., Fan, S.W., Yang, Z., Assouar, B., 2021. Elastic bound state in the continuum with perfect mode conversion. *Journal of the Mechanics and Physics of Solids* 154, 104502. URL: <https://www.sciencedirect.com/science/article/pii/S0022509621001708>, doi:10.1016/j.jmps.2021.104502.
- Chai, Y., Yao, S., Yang, X., Li, Y., 2023. Asymmetric full mode-converting transmission of elastic waves. *New Journal of Physics* 25, 053027. URL: <https://dx.doi.org/10.1088/1367-2630/acd0cf>, doi:10.1088/1367-2630/acd0cf. publisher: IOP Publishing.
- Chaplain, G.J., De Ponti, J.M., Colombi, A., Fuentes-Dominguez, R., Dryburg, P., Pieris, D., Smith, R.J., Clare, A., Clark, M., Craster, R.V., 2020. Tailored elastic surface to body wave Umklapp conversion. *Nature Communications* 11, 3267. URL: <https://www.nature.com/articles/s41467-020-17021-x>, doi:10.1038/s41467-020-17021-x. publisher: Nature Publishing Group.
- Chen, S., Zhang, Y., Hao, C., Lin, S., Fu, Z., 2014. Functionally graded materials for impedance matching in elastic media. *Physics Letters A* 378, 77–81. URL: <https://www.sciencedirect.com/science/article/pii/S0375960113010074>, doi:10.1016/j.physleta.2013.10.040.
- Chen, Y., Hu, G., 2019. Broadband and High-Transmission Metasurface for Converting Underwater Cylindrical Waves to Plane Waves. *Physical Review Applied* 12, 044046. URL: <https://link.aps.org/doi/10.1103/PhysRevApplied.12.044046>, doi:10.1103/PhysRevApplied.12.044046. publisher: American Physical Society.
- Clement, G.T., White, P.J., Hynynen, K., 2004. Enhanced ultrasound transmission through the human skull using shear mode conversion. *The Journal of the Acoustical Society of America* 115, 1356–1364. URL: <https://doi.org/10.1121/1.1645610>, doi:10.1121/1.1645610.
- Colombi, A., Ageeva, V., Smith, R.J., Clare, A., Patel, R., Clark, M., Colquitt, D., Roux, P., Guenneau, S., Craster, R.V., 2017. Enhanced sensing and conversion of ultrasonic Rayleigh waves by elastic metasurfaces. *Scientific Reports* 7, 6750. URL: <https://www.nature.com/articles/s41598-017-07151-6>, doi:10.1038/s41598-017-07151-6. publisher: Nature Publishing Group.

- Dal Poggetto, V.F., Bosia, F., Urban, D., Beoletto, P.H., Torgersen, J., Pugno, N.M., Gliozzi, A.S., 2023. Cochlea-inspired tonotopic resonators. *Materials & Design* 227, 111712. URL: <https://www.sciencedirect.com/science/article/pii/S0264127523001272>, doi:10.1016/j.matdes.2023.111712.
- Ding, T., Song, A., Sun, C., Xiang, Y., Xuan, F.Z., 2022. Mode conversion of Lamb waves in a composite phononic crystal plate: Numerical analysis and experimental validation. *Journal of Applied Physics* 132, 225103. URL: <https://doi.org/10.1063/5.0124089>, doi:10.1063/5.0124089.
- Dorn, C., Kochmann, D.M., 2022. Ray theory for elastic wave propagation in graded metamaterials. *Journal of the Mechanics and Physics of Solids* 168, 105049. URL: <https://www.sciencedirect.com/science/article/pii/S0022509622002277>, doi:10.1016/j.jmps.2022.105049.
- Dorn, C., Kochmann, D.M., 2023. Conformally graded metamaterials for elastic wave guidance. *Extreme Mechanics Letters* 65, 102091. URL: <https://www.sciencedirect.com/science/article/pii/S2352431623001372>, doi:10.1016/j.eml.2023.102091.
- Fletcher, N.H., Thwaites, S., 1992. Multi-horn matching plate for ultrasonic transducers. *Ultrasonics* 30, 67–75. URL: <https://www.sciencedirect.com/science/article/pii/0041624X9290036L>, doi:10.1016/0041-624X(92)90036-L.
- Gerard, N.J., Cui, H., Shen, C., Xie, Y., Cummer, S., Zheng, X., Jing, Y., 2019. Fabrication and experimental demonstration of a hybrid resonant acoustic gradient index metasurface at 40 kHz. *Applied Physics Letters* 114, 231902. URL: <https://doi.org/10.1063/1.5095963>, doi:10.1063/1.5095963.
- Guo, Y., 2025. Directional sound propagation in acoustic artificial structures. *npj Acoustics* 1, 8. URL: <https://www.nature.com/articles/s44384-025-00009-6>, doi:10.1038/s44384-025-00009-6. publisher: Nature Publishing Group.
- He, X., Dong, H.W., Ren, Z., Zhao, S.D., Wang, K., Hu, Y., Xiang, P., Li, Y., Chen, M., Fang, D., 2023. Inverse-designed single-phase elastic metasurfaces for underwater acoustic vortex beams. *Journal of the Mechanics and Physics of Solids* 174, 105247. URL: <https://www.sciencedirect.com/science/article/pii/S0022509623000510>, doi:10.1016/j.jmps.2023.105247.
- Hintze, J.L., Nelson, R.D., 1998. Violin Plots: A Box Plot-Density Trace Synergism. *The American Statistician* 52, 181–184. URL: <https://www.tandfonline.com/doi/abs/10.1080/00031305.1998.10480559>, doi:10.1080/00031305.1998.10480559. publisher: ASA Website _eprint: <https://www.tandfonline.com/doi/pdf/10.1080/00031305.1998.10480559>.
- Jiang, M., Zhou, H.T., Zhu, T., Wang, Y.F., Assouar, B., Wang, Y.S., 2025. Impedance theory-based elastic metasurface enabling precise mode conversion and preservation. *Journal of the Mechanics and Physics of Solids* 203,

106231. URL: <https://www.sciencedirect.com/science/article/pii/S0022509625002078>, doi:10.1016/j.jmps.2025.106231.
- Jiang, X., Liang, B., Zou, X.y., Yin, L.l., Cheng, J.c., 2014. Broadband field rotator based on acoustic metamaterials. *Applied Physics Letters* 104, 083510. URL: <https://aip.scitation.org/doi/10.1063/1.4866333>, doi:10.1063/1.4866333. publisher: American Institute of Physics.
- Jin, Y., Djafari-Rouhani, B., Torrent, D., 2019. Gradient index phononic crystals and metamaterials. *Nanophotonics* 8, 685–701. URL: <https://www.degruyter.com/document/doi/10.1515/nanoph-2018-0227/html>, doi:10.1515/nanoph-2018-0227. publisher: De Gruyter.
- Kim, S.Y., Oh, Y.B., Lee, J.S., Kim, Y.Y., 2023. Anomalous mode-converting reflection of elastic waves using strip-type metagratings. *Mechanical Systems and Signal Processing* 186, 109867. URL: <https://www.sciencedirect.com/science/article/pii/S0888327022009359>, doi:10.1016/j.ymsp.2022.109867.
- Lee, J., Kweun, M., Lee, W., Il Park, C., Kim, Y.Y., 2022. Perfect transmission of elastic waves obliquely incident at solid-solid interfaces. *Extreme Mechanics Letters* 51, 101606. URL: <https://www.webofscience.com/api/gateway?GWVersion=2&SrcAuth=DOI&SrcApp=WOS&KeyAID=10.1016%2Fj.eml.2022.101606&DestApp=DOI&SrcAppSID=USW2EC0B63GZk8HoFxsDmitDxiyci&SrcJTitle=EXTREME+MECHANICS+LETTERS&DestDOIRegistrantName=Elsevier>, doi:10.1016/j.eml.2022.101606. place: Amsterdam Publisher: Elsevier WOS:000819921400008.
- Lee, J., Kweun, M.J., Lee, W., Seung, H.M., Kim, Y.Y., 2024a. Perfect circular polarization of elastic waves in solid media. *Nature Communications* 15, 992. URL: <https://www.nature.com/articles/s41467-024-45146-w>, doi:10.1038/s41467-024-45146-w. publisher: Nature Publishing Group.
- Lee, W., Lee, J., Park, C.I., Kim, Y.Y., 2024b. Polarization-independent full mode-converting elastic metasurfaces. *International Journal of Mechanical Sciences* 266, 108975. URL: <https://www.sciencedirect.com/science/article/pii/S0020740324000183>, doi:10.1016/j.ijmecsci.2024.108975.
- Lin, X.Y., Li, E., He, Z.C., Wu, Y., Li, Q.Q., 2021. Design of single-phase chiral metamaterials for broadband double negativity via shape optimization. *Applied Mathematical Modelling* 91, 335–357. URL: <https://www.sciencedirect.com/science/article/pii/S0307904X2030562X>, doi:10.1016/j.apm.2020.09.041.
- Liu, C., Luo, J., Lai, Y., 2018. Acoustic metamaterials with broadband and wide-angle impedance matching. *Physical Review Materials* 2, 045201. URL: <https://link.aps.org/doi/10.1103/PhysRevMaterials.2.045201>, doi:10.1103/PhysRevMaterials.2.045201. publisher: American Physical Society.
- Liu, Z., Shan, S., Zhang, C., Cheng, L., 2025. Effective generation of shear horizontal waves from Lamb waves by meta-converters. *Mechanical Systems and Signal Processing* 241, 113516. URL: <https://www.sciencedirect.com/science/article/pii/S0888327025012178>, doi:10.1016/j.ymsp.2025.113516.

- Mazzotti, M., Kohtanen, E., Erturk, A., Ruzzene, M., 2022. Identification of Critical Angles in Shear Mode Conversion-Based Transcranial Ultrasound via Leaky Guided Wave Analysis, in: 2022 IEEE International Ultrasonics Symposium (IUS), pp. 1–4. URL: <https://ieeexplore.ieee.org/document/9958552>, doi:10.1109/IUS54386.2022.9958552. ISSN: 1948-5727.
- Miao, H., Li, F., 2021. Shear horizontal wave transducers for structural health monitoring and nondestructive testing: A review. *Ultrasonics* 114, 106355. URL: <https://www.sciencedirect.com/science/article/pii/S0041624X21000032>, doi:10.1016/j.ultras.2021.106355.
- Ogren, A.C., Feng, B.T., Bouman, K.L., Daraio, C., 2024. Gaussian process regression as a surrogate model for the computation of dispersion relations. *Computer Methods in Applied Mechanics and Engineering* 420, 116661. URL: <https://www.sciencedirect.com/science/article/pii/S0045782523007843>, doi:10.1016/j.cma.2023.116661.
- Piao, C., Yang, X., Kweun, J.M., Kim, H., Park, H., Cho, S.H., Kim, Y.Y., 2020. Ultrasonic flow measurement using a high-efficiency longitudinal-to-shear wave mode-converting meta-slab wedge. *Sensors and Actuators A: Physical* 310, 112080. URL: <https://www.sciencedirect.com/science/article/pii/S092442472030412X>, doi:10.1016/j.sna.2020.112080.
- Rathod, V.T., 2020. A Review of Acoustic Impedance Matching Techniques for Piezoelectric Sensors and Transducers. *Sensors* 20, 4051. URL: <https://www.mdpi.com/1424-8220/20/14/4051>, doi:10.3390/s20144051. publisher: Multidisciplinary Digital Publishing Institute.
- Sarvazyan, A.P., Rudenko, O.V., Swanson, S.D., Fowlkes, J.B., Emelianov, S.Y., 1998. Shear wave elasticity imaging: a new ultrasonic technology of medical diagnostics. *Ultrasound in Medicine & Biology* 24, 1419–1435. doi:10.1016/s0301-5629(98)00110-0.
- Shi, J., 2018. Dominant phonon polarization conversion across dimensionally mismatched interfaces: Carbon-nanotube–graphene junction. *Physical Review B* 97. doi:10.1103/PhysRevB.97.134309.
- Smith, D.R., Mock, J.J., Starr, A.F., Schurig, D., 2005. Gradient index metamaterials. *Physical Review E* 71, 036609. URL: <https://link.aps.org/doi/10.1103/PhysRevE.71.036609>, doi:10.1103/PhysRevE.71.036609. publisher: American Physical Society.
- Taljanovic, M.S., Gimber, L.H., Becker, G.W., Latt, L.D., Klauser, A.S., Melville, D.M., Gao, L., Witte, R.S., 2017. Shear-Wave Elastography: Basic Physics and Musculoskeletal Applications. *Radiographics* 37, 855–870. URL: <https://www.ncbi.nlm.nih.gov/pmc/articles/PMC5452887/>, doi:10.1148/rg.2017160116.
- Wallen, S.P., Boechler, N., 2017. Shear to longitudinal mode conversion via second harmonic generation in a two-dimensional microscale granular crystal. *Wave Motion* 68, 22–30. URL: <https://www.sciencedirect.com/science/article/pii/S0165212516301019>, doi:10.1016/j.wavemoti.2016.08.009.

- Wang, L., Wang, L., Lin, Y., Lu, X., Zhao, C., 2021. Transfer matrix model and experimental validation for a radial-torsional ultrasonic motor. *Mechanical Systems and Signal Processing* 160, 107897. URL: <https://www.sciencedirect.com/science/article/pii/S0888327021002922>, doi:10.1016/j.ymsp.2021.107897.
- Wang, Y., Cai, Y., Gong, H., Lee, Y.S., 2022. Design and 3D printing of waveguide-based ultrasonic longitudinal-torsional transducers for medical needle insertion. *Sensors and Actuators A: Physical* 344, 113706. URL: <https://www.sciencedirect.com/science/article/pii/S0924424722003442>, doi:10.1016/j.sna.2022.113706.
- White, R.S., Stephen, R.A., 1980. Compressional to shear wave conversion in oceanic crust. *Geophysical Journal International* 63, 547–565. URL: <https://doi.org/10.1111/j.1365-246X.1980.tb02637.x>, doi:10.1111/j.1365-246X.1980.tb02637.x.
- Xu, Y., Gu, C., Hou, B., Lai, Y., Li, J., Chen, H., 2013. Broadband asymmetric waveguiding of light without polarization limitations. *Nature Communications* 4, 2561. URL: <https://www.nature.com/articles/ncomms3561>, doi:10.1038/ncomms3561. publisher: Nature Publishing Group.
- Yang, S., Rufo, J., Chen, Y., Chen, C., Drinkwater, B.W., Lee, L.P., Huang, T.J., 2025. Acoustic tweezers for advancing precision biology and medicine. *Nature Reviews Methods Primers* 5, 49. URL: <https://www.nature.com/articles/s43586-025-00415-w>, doi:10.1038/s43586-025-00415-w. publisher: Nature Publishing Group.
- Yang, X., Kim, Y.Y., 2018a. Asymptotic theory of bimodal quarter-wave impedance matching for full mode-converting transmission. *Physical Review B* 98, 144110. URL: <https://link.aps.org/doi/10.1103/PhysRevB.98.144110>, doi:10.1103/PhysRevB.98.144110.
- Yang, X., Kim, Y.Y., 2018b. Topology optimization for the design of perfect mode-converting anisotropic elastic metamaterials. *Composite Structures* 201, 161–177. URL: <https://www.sciencedirect.com/science/article/pii/S0263822318301090>, doi:10.1016/j.compstruct.2018.06.022.
- Yang, X., Kweun, M., Kim, Y.Y., 2019. Monolayer metamaterial for full mode-converting transmission of elastic waves. *Applied Physics Letters* 115, 071901. URL: <https://aip.scitation.org/doi/10.1063/1.5109758>, doi:10.1063/1.5109758. publisher: American Institute of Physics.
- Yi, J., Meng, Z., Chen, J., Chen, C.Q., 2023. Dispersive higher harmonic generation and enhancement in mechanical metamaterials. *International Journal of Mechanical Sciences* 246, 108146. URL: <https://www.sciencedirect.com/science/article/pii/S0020740323000486>, doi:10.1016/j.ijmecsci.2023.108146.
- Zelhofer, A.J., Kochmann, D.M., 2017. On acoustic wave beaming in two-dimensional structural lattices. *International Journal of Solids and Structures* 115–116, 248–269. URL: <https://www.sciencedirect.com/science/article/pii/S0020768317301336>, doi:10.1016/j.ijsolstr.2017.03.024.

Zheng, M., Park, C.I., Liu, X., Zhu, R., Hu, G., Kim, Y.Y., 2020. Non-resonant metasurface for broadband elastic wave mode splitting. *Applied Physics Letters* 116, 171903. URL: <https://aip.scitation.org/doi/10.1063/5.0005408>, doi:10.1063/5.0005408. publisher: American Institute of Physics.

Zorzetto, L., Andena, L., Briatico-Vangosa, F., De Noni, L., Thomassin, J.M., Jérôme, C., Grossman, Q., Mertens, A., Weinkamer, R., Rink, M., Ruffoni, D., 2020. Properties and role of interfaces in multimaterial 3D printed composites. *Scientific Reports* 10, 22285. URL: <https://www.nature.com/articles/s41598-020-79230-0>, doi:10.1038/s41598-020-79230-0. publisher: Nature Publishing Group.